Available online at www.sciencedirect.com
ScienceDirect
Journal of Nuclear Materials 372 (2008) 94–105
journal of nuclear materials
www.elsevier.com/locate/jnucmat

Fission-enhanced diffusion in dispersion fuels

D. Olander

Department of Nuclear Engineering, University of California, Berkeley, CA, 94707, United States

Received 6 September 2006; accepted 13 February 2007

Abstract

Irradiation-induced diffusion in finite, two-phase systems is analyzed and applied to the geometry of dispersion fuels of the type used in research and test reactors. A fissioning sphere irradiates the surrounding medium in which fission also takes place. In place of the fission rate used in conventional irradiation-induced diffusion coefficient (D^*) correlations, the energy deposition rates due to electronic and nuclear stopping of the fission fragments are separated. The former is used to drive the point-defect contribution to D^* and the latter is the source of the thermal-spike component. This separation accounts for the preponderance of electronic energy loss early in the track of a fission-fragment and the dominance of nuclear stopping near the end of the range. This distinction accounts for the difference in the relative intensities of these two energy loss modes in a fission-fragment that exits one phase and deposits energy in an adjacent medium in which D^* is to be determined. Fission-fragment stopping powers and projected ranges are obtained from SRIM software, thereby permitting extraction of the two types of energy deposition rates from the fission rate. As expected, the ratio of nuclear stopping to electronic stopping in the medium surrounding a fissioning inclusion increases with distance from the interface. The effective irradiation-enhanced diffusivity for use in the diffusion equation depends upon two parameters: the fraction of D^* in an infinite, homogeneous solid attributable to nuclear stopping and the ratio of the volumetric fission rates in the dispersed and continuous phases.

1. Introduction

Most research and test reactors around the world operate on dispersion fuels, by which is meant a two-phase mixture of spherical particles a U, Mo alloy (the dispersed phase) in a matrix of a high-thermal conductivity material such as aluminum (the continuous phase). Another example is the fuel of TRIGA reactors, in which uranium spheres constitute the dispersed phase embedded in a continuous phase of zirconium hydride. Because of proliferation concerns, there is an ongoing effort to replace fuels using high-enriched uranium (HEU, ~90% ^{235}U) with low-enriched uranium (LEU, <20% ^{235}U). The technical challenge in realizing this switch is packing the same amount of ^{235}U formerly in HEU fuel into fuel utilizing LEU without changing the dimensions of the fuel element and maintaining the same power density. Early TRIGA reactors, for example, utilized a dispersion fuel consisting of 8 wt% HEU in a matrix of zirconium hydride. After conversion, the fuel contains 45 wt% LEU.

One of the problems encountered in developing the U, Mo/Al fuel is reaction between the dispersed phase and the matrix phase. The irreversible reaction

$$(U, Mo) + 3Al \rightarrow (U, Mo)Al_3$$

takes place at the surface of the U, Mo sphere, which is converted to the aluminide reaction product. The kinetics are believed to be controlled by the diffusion of Al from the matrix through the reaction product to the interface between the shrinking U, Mo sphere and the growing reaction-product annulus around it (Fig. 1). The aluminide has a substantially-lower thermal conductivity than either of the metals, and its presence causes the U, Mo to heat up and release fission-gas faster than in the absence of the reaction product. Because of the intense fission-fragment (ff) bombardment of the aluminide and the low temperature (<~300 °C), Al transport in the reaction product is due entirely to irradiation diffusion; thermally-activated diffusion is negligible.

0022-3115/$ - see front matter © 2007 Published by Elsevier B.V.
doi:10.1016/j.jnucmat.2007.02.014

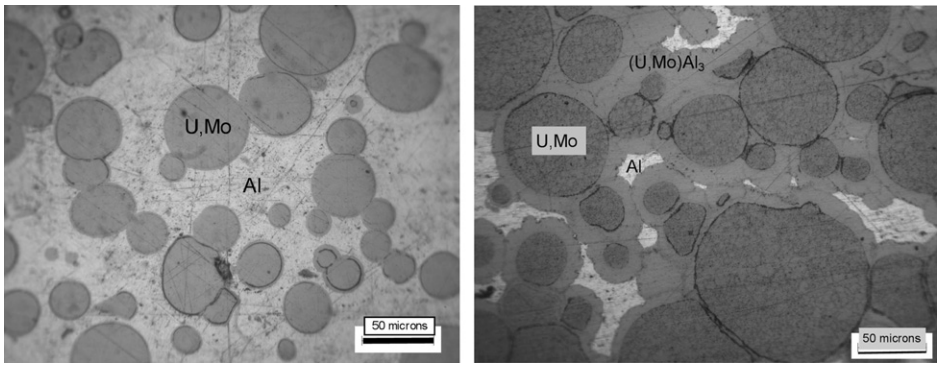

Fig. 1. U, Mo spheres dispersed in an aluminum matrix (left) with (U, Mo)Al_3 reaction product (right). (Courtesy of the RERTR Program – Idaho Nat'l Laboratory and Argonne Nat'l Laboratory.)

It is generally accepted that there are two components of the irradiation diffusion coefficient (D^*), each associated with a mode of fission damage. A frequently-used correlation contains two terms reflecting this distinction [1].

$$D^* = D_e^* + D_n^*, \tag{1}$$

where D_e^* is the contribution attributed to electronic stopping in the thermal-spike created by a fission-fragment (ff) and D_n^* is associated with vacancies and interstitials created by knock-on cascades produced by nuclear stopping. These point defects remain in the lattice long after the fission event.

The objectives of this paper are to: (i) quantitatively associate the thermal-spike component with electronic stopping and the point-defect term with nuclear stopping; (ii) calculate each component of D^* in a spherically-symmetric, two-phase geometry; and (iii) analyze the effect of the position-dependent D^* on the kinetics of a diffusion-controlled reaction in the same geometry.

1.1. Radiation-induced diffusion

In an infinite, homogeneous medium, both components of D^* are expressed as functions of the fission rate $\dot{F}$. In this case, the portion of fission energy appearing as electronic excitation is the same everywhere, so the intensity of electronic-energy deposition is simply proportional to $\dot{F}$ (the same is true for energy deposition by nuclear stopping). In a two-phase medium, however, the separation must be made explicit. This is accomplished by relating each mode of energy deposition to the stopping power for that mode.

Fission energy is partitioned into the two energy deposition rates

$$E_{ff}\dot{F} = \dot{E}_e + \dot{E}_n, \tag{2}$$

where E_{ff} is the birth-energy of a ff and $\dot{E}_e$ and $\dot{E}_n$ are the rates per unit volume of energy deposition by electronic stopping and nuclear stopping, respectively. In Appendix A, the relations of these quantities to the stopping powers are shown to be

$$\dot{E}_e = \dot{F}\int_0^{\mu} S_e dr \text{ and } \dot{E}_n = \dot{F}\int_0^{\mu} S_n dr, \tag{3}$$

Table 1
Radiation damage in UO_2 (from Refs. [2,3])

Property	Light ff	Heavy ff
Energy, E_{ff}, MeV	95	67
Range in UO_2, μm	9	7
% of E_{ff} into nuclear stopping	3	5
O displacement energy, eV	20	20
U displacement energy, eV	40	40
O defects produced	2.8×10^4	4.5×10^4
U defects produced	1.0×10^4	1.6×10^4

where S_e and S_n are the energy-dependent stopping powers[1] and μ is the range of the ff. Characteristics of the fission fragments produced by ^{235}U fission and their effects on the UO_2 lattice (for which data are most plentiful) are given in Table 1. The third row of this table indicates that the nuclear stopping contribution is 3–5% of the total energy deposition rate.

In the dispersion fuel both D_e^* and D_n^* are position-dependent; a ff created in the U, Mo sphere (region 1) deposits some of its energy in this phase, but the balance in the aluminide annulus (region 2). Since electronic stopping is dominant at high energies and nuclear stopping at low energies, the ratio of the rates of energy deposition by the two mechanisms at the end of the range is different from that close to the fission event.

The fission rates in the two regions are $\dot{F}_2$ and $\dot{F}_1$, respectively. The calculation is broken into two parts. The first is the contribution of ffs originating in region 1 that stop in region 2. The second is the contribution of ffs originating in region 2 that deposit all or part of their energy in this phase. The effect of ffs emanating from the sphere is limited to an annulus in region 2 of a thickness equal to the range of ffs in the latter material (μ_2). If the thickness of the reaction product layer is greater than μ_2, region 2 is effectively infinite.

The method consists of replacing the fission rate in the correlation of D^* [1] by the electronic-energy deposition

[1] $S_i = -(dE_{ff}/dx)_i$, where i = e or n.

rate $\dot{E}_e$ in the thermal-spike component and by the nuclear energy deposition rate $\dot{E}_n$ in the point-defect term.

1.2. The thermal-spike or electronic stopping mechanism

As discussed in Refs. [2–5], the principal effect of irradiation on diffusivities is due to the 'thermal-spike' that accompanies the track of a fission-fragment. The mechanism is electronic excitation by the moving ion, which results in intense heating in the immediate vicinity of the fission track as the electrons return to their ground states. Because of the locally high temperatures, ordinary thermally-activated diffusion of all species in the material is increased for a short period in a small volume. The pressure pulse that accompanies the volume change due to heating (and probably melting) a small rod of the material also contributes to the enhanced mobility. In UO_2, calculations show that the transient temperature distribution exceeds the melting point over a volume of $\sim 1.5 \times 10^{-16}\,cm^3$ for about 2×10^{-11} s. Averaged over the range of the ff, melting occurs out to a radius of 2.4 nm around the ff track.

Experiments show that the diffusivity enhancement of U in UO_2, UC, and UN due to electronic excitation is proportional to the fission rate

$$D_e^* = A \times \dot{F}, \tag{4}$$

where the diffusivity is in cm^2/s, the fission density in $cm^{-3}\,s^{-1}$. The constant of proportionality in Eq. (4) depends on the material, and probably the diffusing species as well. In ceramics, the latter include the cations, the anions and any impurity atoms. For U in UO_2 $A = 1.5 \times 10^{-29}\,cm^5$ [4,5]. For U in UC, A is about a fifth of the UO_2 value, and A for U in UN about a tenth of that for UO_2. The relative magnitudes of these A values vary inversely with the thermal conductivities, an observation that supports the thermal-spike model; the higher the thermal conductivity, the more rapidly heat produced by electronic stopping is dissipated and the lower are the temperatures around the ff track. The comparable quantities for the coefficient A in the nonmetals in these ceramics have not been reported.

For a typical radiation-produced impurity (Xe in UO_2), $A = 1.5 \times 10^{-30}\,cm^5$, or an order of magnitude smaller than A for U in UO_2. Assuming this value of A, Eq. (4) becomes

$$D_e^* = 1.5 \times 10^{-30} \dot{F}. \tag{4a}$$

For a fission rate of $4 \times 10^{14}\,cm^{-3}\,s^{-1}$, this formula gives $D_e^* = 6 \times 10^{-16}\,cm^2/s$.

1.3. The 'point-defect' or nuclear stopping mechanism

The augmented population of vacancies and interstitials remaining after the fission event arises from nuclear stopping, whereby energy is transferred to lattice atoms by scattering collisions with the moving ff. Table 1 shows that the number of point defects produced is proportional to the percentage of the initial ff energy that goes into nuclear stopping. Some of the vacancies and interstitials produced by ion–atom collisions escape recombination and remain in the solid after the cascade has subsided. Their presence accelerates diffusion of all species whose migration mechanism involves point defects.

Because of the low temperatures involved, removal of these point defects is dominated by recombination, with negligible trapping at microstructural sinks. The point-defect balances for vacancies and interstitials are identical. By analogy to neutron-irradiated metals [Sec. 19.5.10] of Ref. [6], the point-defect balances become

$$K = k_{rec} x_V x_I \text{ and } x_V = x_I, \tag{5}$$

where K is the defect production rate in units of displacements-per-atom-per-second, or dpa/s. K is related to the fission rate by

$$K = \alpha \dot{F} \Omega \cong \alpha \dot{F} a_o^3 \tag{6}$$

α is the number of surviving point-defect pairs per fission event, for which a low value $\sim 10^4$ is given in Table 1. Other estimates produce values as high as 5×10^5 [1]. Ω is the volume of an atom (for a metal) or a molecule (for a ceramic). In Eq. (6), it is approximated by the cube of the lattice parameter, a_o.

x_I and x_V in Eq. (5) are the interstitial and vacancy fractions on the lattice sites. k_{rec} is the rate constant for recombination [Sec. 13.4.2] of Ref. [6]:

$$k_{rec} = \frac{z D_I}{a_o^2} = z j_I, \tag{7}$$

where z is the number of lattice sites in which annihilation of a vacancy by an intersititial is certain. Because $D_I \gg D_V$, the mechanism assumes stationary vacancies and mobile interstitials. Thus, only the diffusivity of the interstitials, D_I, appears in Eq. (7). To arrive at the second form of k_{rec} in Eq. (7), the interstitial diffusivity has been expressed by the Einstein equation, $a_o^2 j_I$, where a_o is the jump distance (assumed equal to a lattice constant) and j_I is the jump frequency of the interstitial [see Sec. 7.4.2] of Ref. [6] for the analogous derivation of D_V]. According to absolute reaction-rate theory [Sec. 7.5] of Ref. [6], the interstitial jump frequency can be written as:

$$j_I = \nu_I \exp(s_I^m/k) \exp(-\varepsilon_I^m/RT) \tag{8}$$

s_I^m and ε_I^m are the entropy and activation energy associated with the motion of the point-defect and ν_I is the interstitial vibration frequency in its equilibrium site. R is the gas constant.

Migration of the atoms (cation, anion, or impurity) most commonly occurs by the vacancy mechanism, so the nuclear stopping component of D^* is expressed by

$$D_n^* = a_o^2 j_V x_V, \tag{9}$$

where j_V is the jump frequency of the vacancy from a lattice site into an adjacent one. It is given by Eq. (8) with subscript I replaced by V. The site fraction of vacancies, x_V,

is the probability that a vacant site is next to a diffusing atom. With x_V obtained from Eqs. (5)–(8), the nuclear stopping contribution to the diffusivity becomes

$$D_n^* \cong \sqrt{\frac{\alpha}{z}} a_o^{7/2} \sqrt{\nu} \exp\left(-\frac{\varepsilon_V^m - \frac{1}{2}\varepsilon_I^m}{RT}\right)\sqrt{\dot{F}}. \quad (10)$$

The activation entropies are assumed to be zero, or to cancel and the vibration frequencies of the interstitials and vacancies are taken to be equal. To obtain a representative value of D_n^* the following quantities are assumed

$\nu = 10^{13}\ s^{-1}$; $\varepsilon_I^m = 10$ kcal/mol; $\varepsilon_V^m = 20$ kcal/mol;

$T = 600$ K; $\alpha = 5 \times 10^5$; $z = 10$;

$a_o = 4 \times 10^{-8}$ cm; $\dot{F} = 4 \times 10^{14}\ cm^{-3}\ s^{-1}$.

Substituting these values into Eq. (10) gives $D_n^* \sim 7 \times 10^{-16}\ cm^2/s$, which is of the same order of magnitude as D_e^*. However, in view of the sensitivity of D_n to several of the parameters in Eq. (10) (particularly the migration activation energies, temperature and jump distance), the above value of this diffusivity component is very uncertain. For the purpose of the present analysis, it suffices to express Eq. (10) by

$$D_n^* = B\sqrt{\dot{F}} \quad (11)$$

with $B = 3.5 \times 10^{-23}\ cm^{7/2}\ s^{-1/2}$. Note that the effect of temperature in Eq. (10) has been neglected. This term may have been responsible for the temperature effect on reaction-product growth evident in Fig. 1.

1.4. Replacement of the fission rate by the energy deposition rates

Calculation of D_e^* and D_n^* proceeds by replacing $\dot{F}$ in Eqs. (4) and (11) with the energy deposition rates using Eq. (3). for electronic stopping Eq. (4) becomes

$$D_e^* = A'\dot{E}_e \quad (12)$$

with

$$A' = A\left[\int_0^\mu S_e dr\right]^{-1}. \quad (13)$$

For nuclear stopping Eq. (11) becomes

$$D_n^* = B'\sqrt{\dot{E}_n} \quad (14)$$

with

$$B' = B\left[\int_0^\mu S_n dr\right]^{-1/2}. \quad (15)$$

In order to apply Eqs. (12) and (14), the coefficients A and B given or estimated in Sections 1.1 and 1.3 are used. The integrals of the stopping powers for the 67 MeV ff in (U, Mo)Al_3 are 60 MeV and 7 MeV for electronic and nuclear stopping, respectively. This information suffices to calculate the coefficients A' and B' in Eqs. (13) and (15):

$$A' = 2.5 \times 10^{-32}\ cm^5/MeV$$

$$B' = 1.3 \times 10^{-23}\ cm^{-7/2}\ s^{-1/2}/MeV^{1/2}. \quad (16)$$

1.5. Use of SRIM

SRIM is an extraordinarily useful piece of software[2] that describes the consequences of the entry of a high-energy ion into a solid [7]. The atomic species in the solid are recognized but the crystal structure is not; the solid has the correct density but is amorphous. SRIM provides two options. The main portion (called TRIM) follows the displacements caused by the primary knock-on atoms (PKAs) in varying degrees of detail. A subsidiary part of the code calculates the properties of the incident ion as it slows down in the solid. This is the part of SRIM that is used in the present study.

An abbreviated example of the SRIM output is shown in Table 2. As functions of ion energy, the table lists the electronic and nuclear stopping powers, from which the integrals in Eq. (3) were obtained. The *projected range* provided by SRIM is best visualized by the following diagram:

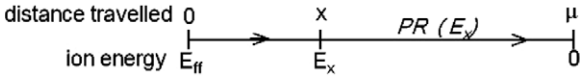

An ion with initial energy E_{ff} penetrates a distance x in a solid, where its energy is E_x. At this energy, the SRIM table gives the projected range $PR(E_x)$. This quantity is related to the range of the full-energy particle, μ, (the last entry of the 4th column) and the distance traveled by

$$\mu = x + PR(E_x). \quad (17)$$

If the distance x is known, entry at $\mu - x$ in the 4th column is the projected, or remaining, range of the particle. However, by reading across to the 1st column, the energy of the ion at penetration distance x is obtained. For example, if the ion initially at 67 MeV moves a distance of 2 μm, its energy is 38.4 MeV. If the medium to the right of location x is different from that to the left, the above energy calculation still applies, but the projected range at x now requires use of the stopping properties of the different medium.

Care is needed for the units. In the calculations that follow, all of the length units are made dimensionless by dividing by μ_1, the range of ffs in region 1 (the U, Mo sphere). Therefore, the units of S must be MeV/length in units to μ_1. All SRIM projected-range (PR) output (in μm) is divided by μ_1. The stopping powers produced by SRIM are in units of keV/μm. Multiplying by 10^{-3} converts keV to MeV and by μ_1 (in μm) changes μm to the length unit used for all other dimensions. The net result is

S (MeV per length in units of μ_1)

$= \mu_1$ (μm) $\times 10^{-3} \times S$ (from SRIM).

[2] Available free on the web at SRIM.org.

Table 2
Abbreviated SRIM stopping output – Xe in $(U_{0.8}Mo_{0.2})Al_3$

SRIM output: xenon in U–Mo–Al
Ion = xenon [54], mass = 132 amu
Target density = 6.9 g/cm^3
Target composition

Atom name	Atomic no.	Atomic percent
U	92	20
Mo	42	5
AI	13	75

Ion energy (MeV)	dE/dx Elec. (keV/μm)	dE/dx Nuclear	Projected range (μm)
0.01	120	1250	0.007
0.03	207	2265	0.013
0.05	268	2558	0.018
0.08	339	2789	0.025
0.12	415	2942	0.033
0.16	479	3016	0.041
0.2	535	3048	0.050
0.3	668	3048	0.069
0.5	867	2928	0.11
1.0	1119	2568	0.21
2.0	1579	2055	0.43
5.0	2818	1346	1.09
10	4427	902	2.04
20	7363	573	3.46
25	8695	491	4.02
30	9896	431	4.51
35	10970	385	4.96
40	11920	350	5.37
45	12780	320	5.76
50	13550	296	6.12
55	14250	276	6.47
60	14900	258	6.80
67	15720	237	7.24

2. Energy deposition rates in the two regions

While an unlimited number of 2-phase, finite medium geometries can be concocted, the sphere in an infinite medium adequately represents the dispersion fuel described in the introduction. The objective here is not to cover all possible geometries and conditions that are pertinent to the analysis of this configuration, which include sphere size relative to ff range, relative fission rates in the two phases and thickness of the annular 'infinite' medium surrounding the sphere. Rather the aim is to demonstrate for a single geometry and one set of conditions how the electronic and nuclear energy depositions rates, and hence the modes of irradiation diffusion that they drive, differ from that of an infinite medium.

The geometry consists of a sphere of radius R (region 1) in which the ff range is μ_1 embedded in a second phase (region 2) in which the ff range is μ_2. Fission occurs in both regions, but at different intensities. The energy deposition rates in region 2 at a variable distance ρ from the center of the sphere (designated as point F) are to be determined. Finite-geometry effects are active only to a distance $R + \mu_2$ from the sphere center; further out, the usual infinite medium analyses apply.

To determine D^* in region 2, the rates of electronic and nuclear energy deposition in this region need to be calculated. For ffs generated in the sphere, most of the energy loss in this region is due to electronic stopping; the major part of the nuclear stopping portion of the ff energy is deposited at the end of the ff track, which is in region 2. Because of this imbalance, the distinction between electronic energy loss and nuclear energy loss must be made explicit, as it is in Eqs. (12) and (14). The energy deposition rates $\dot{E}_e$ and $\dot{E}_n$ at a point in the region 2 can be calculated from the electronic and nuclear stopping powers S_e and S_n. This procedure is described below for ffs originating in the sphere but stopping in the surrounding medium and for ffs originating and stopping in the latter. The analysis consists mainly of detailed geometrical calculations coupled with application of SRIM stopping powers and projected ranges.

The first geometrical problem is the distinction between near and far distances from the center of the sphere representing region 1. This is best shown in Fig. 2 for these two cases. The switch from one diagram to the other occurs at $\rho* = \sqrt{R^2 + \mu_2^2}$.

2.1. $\rho > \rho^*$ (upper diagram in Fig. 2)

At ρ^*, the angle between R and μ_2 at their intersection on the sphere surface is 90°. For larger values of ρ, region 2 consists of two zones feeding point F: zone 2A is an imaginary sphere of radius μ_2 minus the cone with a circular base, where the real and imaginary spheres intersect. This

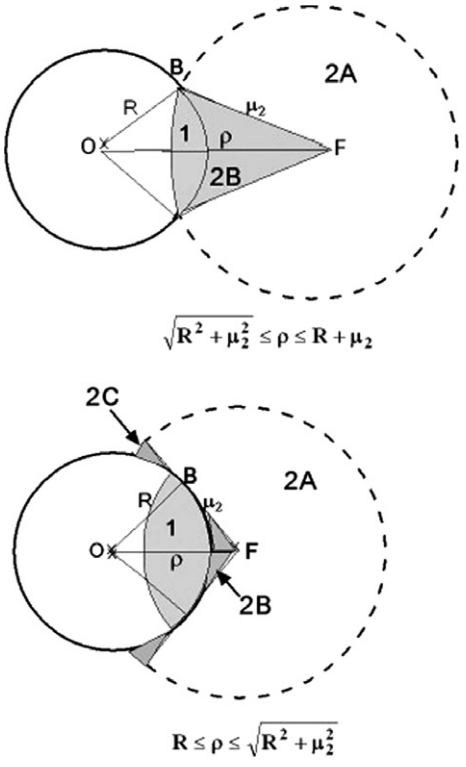

Fig. 2. Geometries of zones supplying ffs to point F.

Table 3
Limits for the radial and angular integrals of the stopping powers

Zone	$R \leqslant \rho \leqslant \sqrt{R^2+\mu_2^2}$				$\sqrt{R^2+\mu_2^2} \leqslant \rho \leqslant R+\mu_2$			
	$(\cos\varphi)_{\min}$	$(\cos\varphi)_{\max}$	$r_{\min}$	$r_{\max}$	$(\cos\varphi)_{\min}$	$(\cos\varphi)_{\max}$	$r_{\min}$	$r_{\max}$
1	X	W	Q_-	Q_+	Y	1	Q_-	Z
	W	1	Q_-	Z				
2A	-1	X	0	μ_2	-1	Y	0	μ_2
2B	X	1	0	Q_-	Y	1	0	Q_-
2C	X	W	Q_+	U	–	–	–	–

$X = \sqrt{1-R^2/\rho^2}$.
$Y = (\mu_2^2+\rho^2-R^2)/2\rho\mu_2$.
$Q_\pm = \rho\cos\varphi \pm \sqrt{R^2-\rho^2\sin^2\varphi}$.
$Z = Q_- + 1 - \mathrm{PR}_1(E_\mathrm{K})$; $\mathrm{PR}_2(E_\mathrm{K}) = Q_-$ (solve for E_K then Z).
$W = \frac{1}{\rho}\sqrt{\rho^2-R^2+\frac{1}{4}[1-\mathrm{PR}_1(E_\mathrm{K})]^2} = \frac{\rho^2-R^2+[\mathrm{PR}_2(E_\mathrm{K})]^2}{2\rho[\mathrm{PR}_2(E_\mathrm{K})]}$; (solve for $E_\mathrm{K}$then W).
$\mathrm{U} = \mu_2 - \mathrm{PR}_2(E_\mathrm{H}) + Q_+$; $\mathrm{PR}_2(E_\mathrm{K}) = Q_-$ (solve for E_K); $\mathrm{PR}_1(E_\mathrm{H}) = \mathrm{PR}_1(E_\mathrm{K}) + Q_+ - Q_-$(solve for E_H then U).

Distances are in units of μ_1; ff energy in MeV
R = radius of region 1.
ρ = distance from center of region 1.
μ_2 = ff range in region 2.
φ = angle from horizontal with origin at point F.
E_K = ff energy upon entering region 2 from region 1.
E_H = energy of ff entering region 1 from region 2.
$\mathrm{PR}_i(E)$ = projected range of ff of energy E in region i.

cone, whose base is a spherical cap, is designated zone 2B. Region 2 needs to be subdivided into these two zones to account for the portion of the imaginary sphere of radius μ_2 that is cut out by region 1. Zone 1 is the portion of the sphere representing region 1 from which ffs can reach point F. Its outer boundary depends on the ranges of the ff in the two media.

2.2. $\rho < \rho^*$ (lower diagram in Fig. 2)

When the location of point F is less than ρ^*, region 2 needs to be divided into three zones. Zones 2A and 2B are the same as in the large-ρ case except that the cone ends at the circle of tangency with the region-1 sphere. The third zone, 2C, includes the portion of region 2 hidden from direct view of point F, but from which ffs can reach this point by passing through medium 1.

2.3. Energy deposition rates

The energy deposition rates at point F due to ffs emitted from any of the zones in the diagrams of Fig. 2 are given by the general formula

$$\frac{\dot{E}}{\dot{F}} = \frac{1}{2}\int_{(\cos\varphi)_{\min}}^{(\cos\varphi)_{\max}} \mathrm{d}(\cos\varphi)\int_{r_{\min}}^{r_{\max}} S\mathrm{d}r. \tag{18}$$

The analysis consists of two determinations, details of which are shown in Appendix B:

- The limits on the two integrals in Eq. (18). The results of this part are summarized in Table 3. For each zone, the integration limits are shown for small-ρ (columns 2–5) and large-ρ (columns 6–9).
- The energy at a point F in region 2 of a ff created in one of the 4 zones. This is determined by the distances traveled by the ff in medium 1 and medium 2 and by the slowing-down properties given by SRIM, as illustrated in Table 2 for the U, Mo alloy constituting region 1.

If region 1 is made of the same material as region 2, the infinite medium solution is recovered. This can be demonstrated by replacing '1' in the equation for Z by μ_2 and PR_1 by PR_2, wherever the former appears in the equations for U and Z. With these substitutions, the sum of the five integrals which correspond to the limits given in Table 3 reduces to Eq. (3).

3. Results

Application of the calculational method to U, Mo-in-Al dispersion fuel is best illustrated by an example. In what follows, all lengths are relative to the range of birth-energy ffs in region 1. For a 67-MeV xenon fission-fragment in $U_{0.8}Mo_{0.2}$, SRIM gives $\mu_1 = 4.16$ μm. Relative to μ_1, the radius of region 1 (the small sphere in Fig. 3) is chosen as $R = 1.2$. According to SRIM, the range of the heavy ff in the $(U_{0.8},Mo_{0.2})Al_3$ reaction product (Region 2) is 7.24 μm, or $\mu_2 = 1.74$ in units of μ_1. Adding this distance to the radius of region 1, the maximum radial reach of the ffs measured from the center of region 1 is 2.94 (in dimensionless terms) or ~12 μm. The fission rates in the two media are $\dot{F}_1 = 2\times10^{14}\,\mathrm{cm^{-3}\,s^{-1}}$ and $\dot{F}_2 = 5\times$

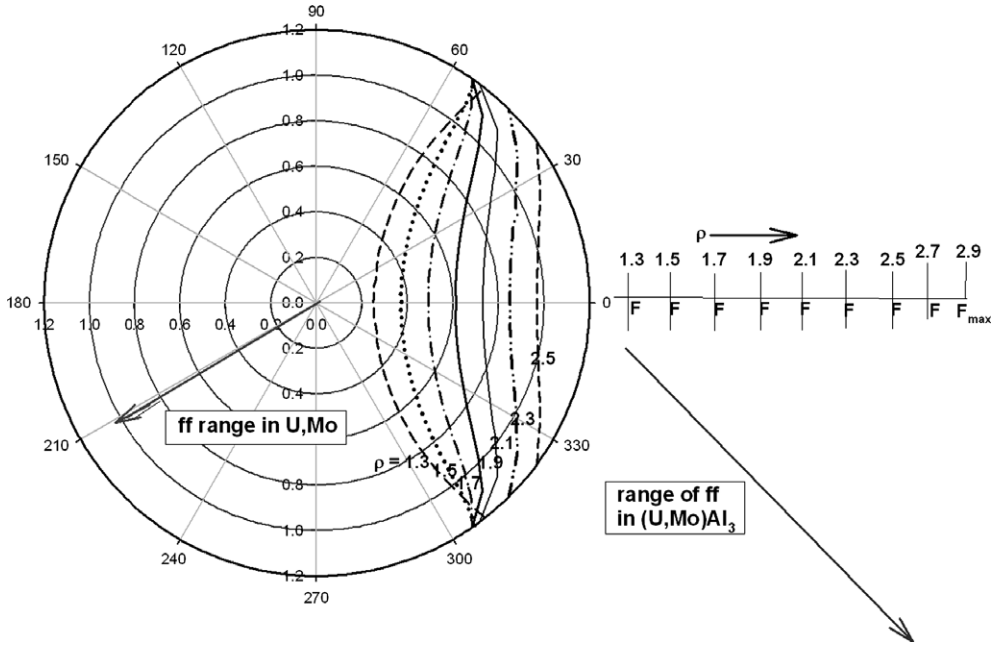

Fig. 3. Integration limits in region 1. All distances are in units of the ff range in $U_{0.8}Mo_{0.2}$.

10^{13} cm^{-3} s^{-1}. These correspond to the uranium densities in the U, Mo alloy and the (U, Mo)Al_3 compound. Ignoring burnup effects, the U/Mo atomic ratio in both media is 4.

3.1. Energy deposition in region 2 from fissions in region 1

The upper radial integration limits r_{max} for zone 1 are shown in the polar plot of Fig. 3 for seven values of ρ, the location of point F (represented by one of the vertical lines on the right). The curves in Fig. 3 separate regions from which a ff can reach a point F (to the right of the curve) from the remainder of the sphere from which a ff stops before reaching point F. The farthest from region 1 that a ff can penetrate region 2 is denoted by F_{max} in Fig. 3. This point is fed only by fissions occurring on the surface of region 1 and emitted at a polar angle of zero.

The energy at point F (E_F) of a ff created at any point within zone 1 is determined by the method described in Appendix B. From this value of E_F, the stopping powers S_e and S_n are obtained from the second and third columns of Table 2. These are then integrated over the range of r and cosφ in Eq. (18) to produce the energy deposition rate relative to the fission rate.

Fig. 4 shows the variation of the two components of $\dot{E}/\dot{F}$ in region 2 with distance from the center of zone 1. For comparison, the horizontal lines represent the infinite, single-phase medium in which the electronic-to-nuclear energy generated per fission is 60/7. In the finite-geometry, the ratio of electronic-to-nuclear energy deposition decreases from ~10 close to the surface of region 1 ($\rho = 1.2$) to ~2 at more remote distances. The reason is straightforward; the ffs originating in region 1 lose energy

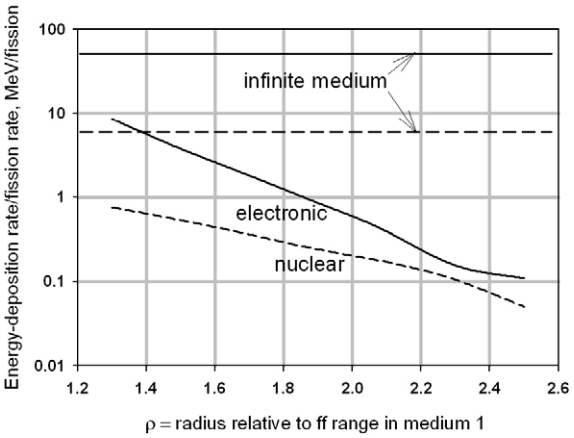

Fig. 4. Electronic (top) and nuclear (bottom) components of the ratios of the energy deposition rates to the fission rates in region 2 due to ffs originating in region 1. The surface of region 1 is located at a relative radius of 1.2.

initially by electronic stopping in region 1, and at the end of their range in region 2, slow down principally by nuclear stopping.

3.2. Energy deposition in region 2 from fissions in both regions

The energy deposition rates in region 2 due to fissions originating in both regions are shown in Figs. 5 and 6, along with the percentage due to ffs from region 1. The total energy deposition rate for each mode is given by

$$\dot{E} = \left(\frac{\dot{E}}{\dot{F}}\right)_1 \dot{F}_1 + \left(\frac{\dot{E}}{\dot{F}}\right)_2 \dot{F}_2. \tag{19}$$

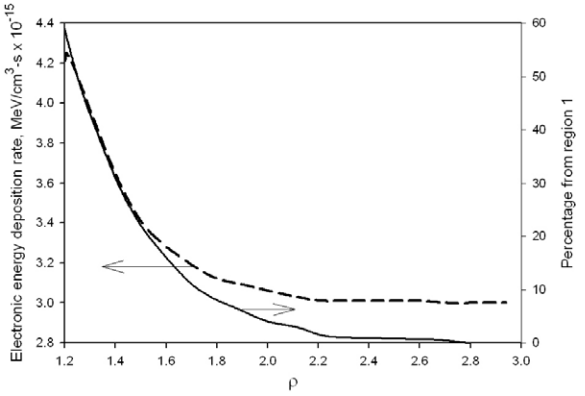

Fig. 5. Electronic-energy deposition rates in region 2 and percentage due to ffs from region 1.

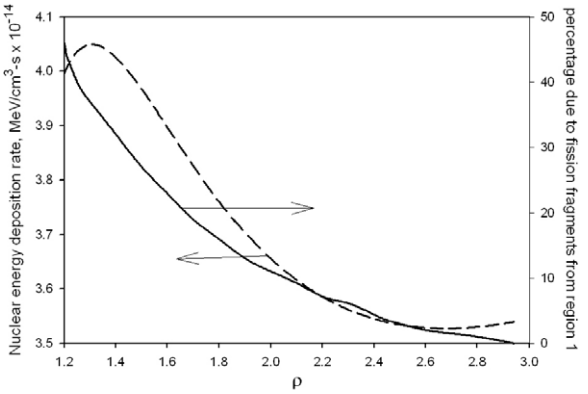

Fig. 6. Nuclear energy deposition rates in region 2 and percentage due to ffs from region 1.

The ratio $(\dot{E}/\dot{F})_1$ for fissions region 1 is taken from Fig. 4 and $(\dot{E}/\dot{F})_2$ for fissions in region 2 is obtained from comparable information calculated for the three zones in region 2 (not shown).

The dashed curves in Figs. 5 and 6 show the variations with distance from the sphere surface of the energy deposition rates from the two mechanisms from all accessible fissioning zones. Both $\dot{E}_e$ and $\dot{E}_n$ decrease, but not as markedly as the factor of 4 ratio of the fission rates in the two media. Over the range of region-1 ffs, $\dot{E}_e$ drops by 30% but $\dot{E}_n$ decreases by only 15%. This is consistent with preponderance of electronic stopping at the beginning of the ff track and nuclear stopping at the end of the track. The ratio of the limiting values of the electronic-to-nuclear dose rates from the same two figures $(3.0\times10^{15}\div 3.55\times10^{14})$ is the same as the $60\div7$ ratio obtained from the stopping power integrals (Section 1.4). Distances for which $\rho>2.8$ corresponds to medium 2 of infinite extent.

The solid curves in Figs. 5 and 6 show the percentage of the total energy deposition rate due to ffs originating in region 1. At the sphere surface, ~60% of the electronic stopping dose rate and ~45% of the nuclear stopping dose rate are due to fissions in region 1. The balance of the dose rates arise from ffs born in region 2. These ratios drop to zero at a distance from the region-1 sphere surface equal to the range of ffs in medium 2. Beyond this distance, the solid receives fission energy only from region 2.

3.3. Diffusion coefficients

Armed with the two energy deposition rates from Figs. 5 and 6 (plus the analogous pair for the energy delivered to region 2 from fissions in region 2), the two components of the irradiation diffusivities can be calculated from Eqs. (12) and (14). The constants in these formulas are given by Eq. (16). In the results are displayed in Fig. 7, the relative magnitude of the two components of D^* is not significant because of the very approximate value of B' used to compute D_n^*.

If $\dot{F}_1=0$, both D_e^* and D_n^* decrease upon moving radially inward. This is the result of the loss of medium 2 in the volume occupied by the nonfissioning sphere.

For $\dot{F}_1/\dot{F}_2=4$, D^* increases as the surface of the sphere is approached. The electronic component of D^* at the sphere surface ($\rho=1.2$) is 40% greater than the bulk value ($\rho=3$). The corresponding enhancement of the nuclear component is 15%. These relatively minor effects are due largely to the compensating effect of the radial dependences of the region 1 and region 2 components of the energy deposition rates; that due to fissions in region 1 drops to zero far from the surface of the sphere (Figs. 5 and 6), while the contribution to $\dot{E}$ at the sphere surface from fissions in region 2 is still about 1/2 that in the bulk material.

3.4. Effect on a diffusion process

The result of interest is not the diffusion coefficients per se, but their effect on the kinetics of diffusion-controlled processes. For this purpose, the transport region is a spherical annulus (region 2) of inner radius $\rho=1.2$ and outer radius $\rho=3.0$. The latter is just beyond the range of ffs

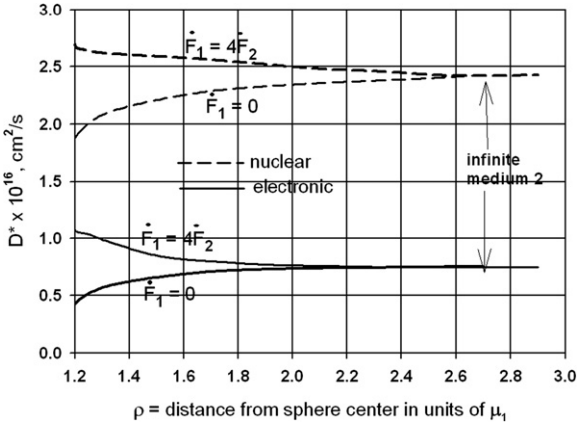

Fig. 7. Irradiation diffusion coefficients in an annulus (region 2) due to energy deposited by fissions in region 2 without fissions in region 1 ($\dot{F}_1=0$) and with fissions in region 1 $\dot{F}_1=4\dot{F}_2$ The surface of the sphere is at $\rho=1.2$.

emitted from the inner sphere (region 1), so the irradiation effects for $\rho > 3$ are those of an infinite medium. The following diffusion problem in this geometry is posed. The spherical annulus initially contains a specified concentration of solute; at time zero, the concentration at the inner surface is reduced to zero; the outer surface is a zero-flux boundary. While this is an artificial problem, the purpose is to demonstrate the effect of the position-dependent D^* in Fig. 7, the components of which are fitted with the formulas:

$$D^*_e = D^*_{e1}\exp(-\lambda_e(\rho - 1.2)) + D^*_{e2},$$
$$D^*_n = D^*_{n1}\exp(-\lambda_n(\rho - 1.2)) + D^*_{n2}. \tag{20}$$

For $\dot{F}_1 = 4\dot{F}$, $\lambda_e = 3.6$ and $\lambda_n = 1.0$. The coefficients $D^*_{e1} + D^*_{e2}$ and $D^*_{n1} + D^*_{n2}$ are the intercepts of the curves at $\rho = 1.2$ and D^*_{e2} and D^*_{n2} are the large-ρ asymptotic values. The total diffusivity in region 2 is the sum of D^*_e and D^*_n

$$D^* = (D^*_{e1} + D^*_{n1})[(1-f)\times\exp(-\lambda_e(\rho - 1.2)) + f \times\exp(-\lambda_n(\rho - 1.2)) + g]. \tag{21}$$

The quantities f and g are

$$f = \frac{D^*_{n1}}{D^*_{e1} + D^*_{n1}} \text{ and } g = \frac{D^*_{e2} + D^*_{n2}}{D^*_{e1} + D^*_{n1}}. \tag{22}$$

The parameter f is a measure of the importance of nuclear stopping in the total irradiation diffusivity at the sphere surface. The parameter g is a measure of the irradiation diffusivity far from the sphere surface to D^* at the sphere surface.

In dimensionless form, the diffusion equation with the diffusivity of Eq. (21) is

$$\frac{\partial C}{\partial \tau} = \frac{1}{\rho^2}\frac{\partial}{\partial \rho}\left\{\rho^2[(1-f)\times\exp(-\lambda_e(\rho - 1.2)) + f \times\exp(-\lambda_n(\rho - 1.2)) + g]\frac{\partial C}{\partial \rho}\right\}, \tag{23}$$

where C is the concentration and $\tau = (D^*_{e1} + D^*_{n1})t/\mu_1^2$ is a dimensionless time.[3] The initial condition is $C = 1$ for all ρ, and the boundary conditions are: $C = 0$ at $\rho = 1.2$ and $\partial C/\partial\rho = 0$ at $\rho = 3.0$. The flux of solute to the central sphere is

$$\text{flux} = (1+g)\left(\frac{\partial C}{\partial \rho}\right)_{\rho=1.2}. \tag{24}$$

Fig. 8 compares the flux variation with time for cases with and without fission in the central sphere. For the former case, $f = 0.5$ and $g = 5$ and the flux at the surface is initially somewhat higher than for the nonfissioning sphere, but these reverse at a later time. The time-integrals of the fluxes are practically equal in the two cases because the final time is long enough to remove essentially all solute initially in the region 2 annulus, irrespective of the magnitude of D^*.

[3] $(D^*_{e1} + D^*_{n1})$ is the value for $\dot{F}_1/\dot{F}_2 = 4$ in both cases.

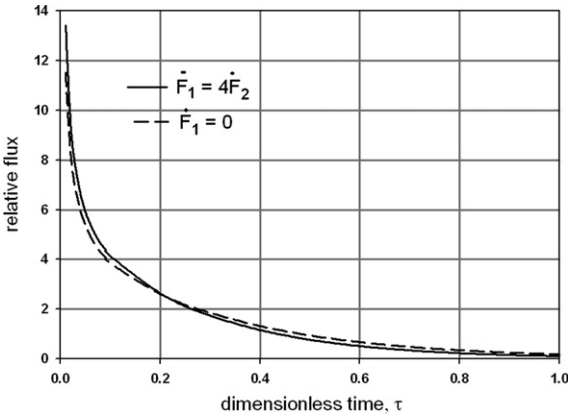

Fig. 8. Effect of a fission in a sphere (region 1) on the solute absorption flux from a surrounding medium (region 2).

4. Conclusions

Irradiation diffusion coefficients developed for infinite homogeneous media have been modified for inhomogeneous two-phase media in which fission occurs in one or both phases. To this end, D^* is separated into two components, D^*_e and D^*_n, representing contributions due to fission-fragment energy deposition by electronic and nuclear stopping, respectively. These two quantities are combined into an effective irradiation diffusivity that depends on the relative magnitudes of D^*_e and D^*_n, which in turn is a function of the ratio of the fission rates in the two phases of the inhomogeneous medium.

The analysis for the U, Mo in Al fuel is applicable to similar dispersion fuels with different materials. Fig. 9 depicts three varieties of dispersion fuels. Each has a spherical fuel particle ranging in diameter from 50–200 μm. Surrounding each is an annulus 8–10 μm wide that is irradiated by fission fragments from the fuel particle. On the left is the system that has been used as a vehicle for the present work.. In addition to the U, Mo alloy fuel sphere, a (U, Mo)Al_3 reaction product annulus of varying thickness also generates fission products, although at a lower rate than the central sphere.

In the center of Fig. 9 is MOX fuel fabricated by mechanically blending powders of PuO_2 and UO_2. After sintering, a compact with a PuO_2 dispersed phase and a UO_2 matrix results. Fission-gas transport in MOX fuel is accelerated in the ff-irradiated layer surrounding the plutonia particles. Very large fuel-to-matrix fission rate ratios would be expected in MOX fuel, with nearly all of the fissions occurring in the plutonia particles rather than in the UO_2 matrix. Fission-gas diffusion from the PuO_2 particles in the surrounding UO_2 in cold regions of the pellet would be significantly affected by the position-dependent D^* exterior to the fuel kernel.

The right-hand diagram in Fig. 9 shows the irradiated zones in the inert-matrix fuel described by Chauvin et al. [8]. In addition to fissioning, ^{241}Am emits alpha-particles, whose range in the matrix is about twice that of the fission

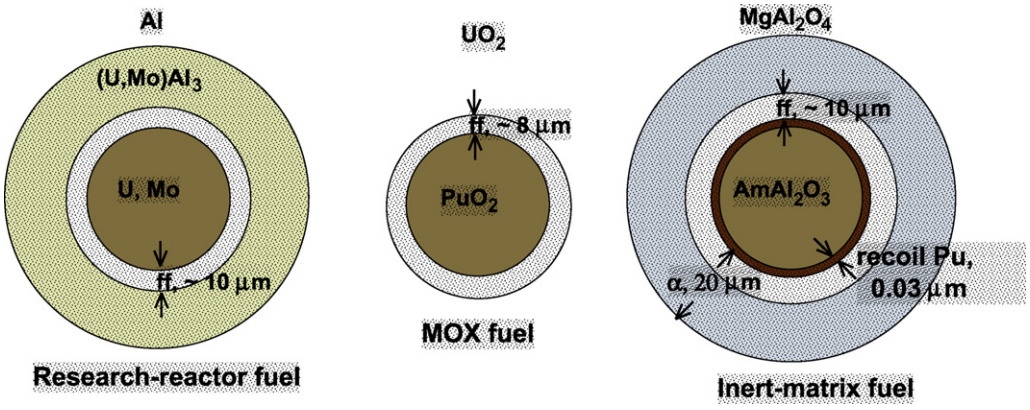

Fig. 9. Three types of dispersion fuels – the central fissile kernel is <100 μm diameter.

fragments. The ^{238}Pu recoil that accompanies the alpha-particle decay process deposits considerable energy in a very narrow band around the fuel particle.

In all three cases shown in Fig. 9, the initial sharp demarcation between the fissile dispersed phase and the nonfissile matrix disappears with burnup. Understanding the kinetics of the growth of the aluminide reaction product at the expense of the U, Mo fuel sphere is the motivation for this work.

During irradiation of MOX fuel, plutonium diffuses into the UO_2 matrix and the initial interface between the two oxides is smeared out. This results in a region similar to the aluminide reaction-product layer in the research-reactor dispersion fuel. Given the chemical similarity of the materials in the dispersed/matrix combination of the inert-matrix fuel in Fig. 9, migration of americium originally in the fuel sphere into the matrix would be expected. All three combinations develop a zone containing the fissile element surrounding the original sphere.

Appendix A. Relation of fission rate to energy deposition rate

In an infinite, homogeneous medium, energy deposition at any point results from slowing-down of ffs originating in a sphere of radius μ, the range of the ffs, around the point. Fig. A1 shows this geometry, with the central point represented by an imaginary sphere of radius s. The probability that a ff produced in the annular volume element $dV = 4\pi r^2 dr$ intersects the central sphere is $\pi s^2/4\pi r^2$. The rate at which ffs from dV intersect the central sphere is

$$d\dot{N} = \frac{\pi s^2}{4\pi r^2}\dot{F}4\pi r^2 dr = \pi s^2 \dot{F} dr.$$

The average distance traveled by the ff in the center sphere is the average chord length, $4/3s$. The energy deposited over this distance is $4/3sS$, where S is the stopping power at the energy of the ff reaching the central sphere. The rate of energy deposition per unit volume in the central sphere due to ffs originating in the annular volume dV is

$$d\dot{E} = \frac{4/3sS}{4/3\pi s^3} d\dot{N} = \frac{S}{\pi s^2}\pi s^2 \dot{F} dr = S\dot{F} dr.$$

Integrating over the radius of the large sphere

$$\frac{\dot{E}}{\dot{F}} = \int_0^{\mu} S dr,$$

which applies independently to electronic and nuclear stopping.

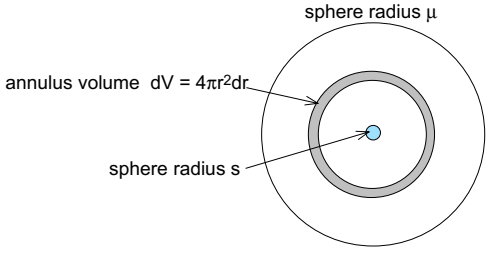

Fig. A1. Geometry for determination of energy deposition from fission in an infinite medium.

Appendix B. Calculation details

Shown here are the detailed steps for computing the energy of a ff at a point in region 2 following passage through portions of one or both phases. The limits of the integrals upon which the energy deposition rate is based are also explained. Medium 1 is a U, Mo alloy sphere with 0.2 atom fraction Mo. The radius of the sphere is 1.2 in units of the ff range in medium 1. Medium 2 is the product of the reaction of medium 1 with aluminum, $(U_{0.8}Mo_{0.2})Al_3$. Enhancement of the diffusion coefficient due to ffs from the central sphere is restricted to an annulus whose thickness is equal to the range of ffs in the reaction product.

B.1. Zone 1, small-ρ

Fig. B1 depicts a ff created at point G heading in the direction of point F. The location of point G is fixed by

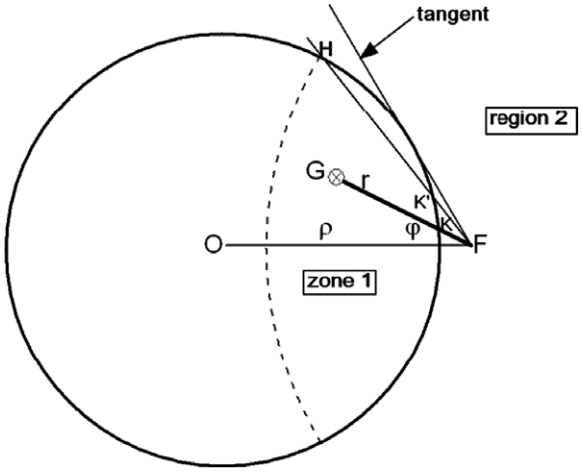

Fig. B1. ff Created at point G in zone 1 and stopping at point F in region 2.

its radial distance r from point F and polar angle φ with respect to reference line FO.

First, the energy E_F at point F of a ff created at point G is determined. The ff travels a distance GK in zone 1 and enters region 2 at point K with energy E_K, which is determined from SRIM. The path length through medium 1 is $GK = r - KF = r - Q_-$, where Q_- is the function of φ given by the third equation in Table 2. GK can also be expressed as the difference in the projected ranges of the ff at point G (equal to the birth-energy range μ_1, or in dimensionless terms, unity) and at point K, written as $PR_1(E_K)$. Equating these two expressions for GK gives

$$PR_1(E_K) = 1 + Q_- - r, \tag{B1}$$

which serves to determine E_K.

After moving the length KF in region 2, the ff energy is determined by $KF = PR_2(E_K) - PR_2(E_F)$, or

$$PR_2(E_F) = PR_2(E_K) - Q_-. \tag{B2}$$

From which E_F is obtained.

The calculation based on Eqs. (B1) and (B2) ceases to apply at a maximum r value for which $E_F = 0$. r_{max} is obtained by setting the left-hand side of Eq. (B2) equal to zero and solving for the corresponding value of E_K. Using this energy in Eq. (B1) gives r_{max} rather than r. This is shown as the symbol Z in Table 2.

The above calculation extends to a maximum φ of $\angle HFO = \cos^{-1} W$, where W is the 5th equation in Table 3. Thereafter, r_{max} follows the arc of the circle rather than the dashed curve in Fig. B1. The segment HF intersects the circle at point K′. The lengths of the segments HF and K′F are Q_+ and Q_-, respectively. $Q_\pm$ is given by the 3rd formula in Table 3 in which $\cos\varphi$ is replaced by W. The travel distance in medium 1, $HK' = HF - K'F = Q_+ - Q_-$. In terms of projected ranges, $K'F = PR_2(E_K)$ because the ff energy at point F is zero, and $HK' = 1 - PR_1(E_K)$. This leads to the equations:

$$1 - PR_1(E_K) = Q_+ - Q_- \text{ and } PR_2(E_K) = Q_-. \tag{B3}$$

When Q_+ and Q_- are express by the 3rd formula in Table 3 and the resulting equations solved for W, the 5th pair of equations in Table 3 is obtained. These must be solved simultaneously for E_K and W.

The maximum angle from which ffs created in zone 1 can reach point F is labeled as the tangent in Fig. A1. The cosine of this maximum angle is denoted by X in Table 3. For polar angles between $\cos^{-1} W$ and $\cos^{-1} X$, r_{min} for zone 1 remains the same (i.e., Q_-) but r_{max} lies along the arc of the circle rather than on the dashed curve. For polar angles in this range, $r_{max} = Q_+$.

B.2. Zone 1, large-ρ

In this range of ρ, there is no discontinuity in the formula for r_{max} as there is in the small-ρ range analyzed above. r_{max} is given by the method labeled Z in Table 2. Only the maximum angle formula differs from that in the small-ρ range; X is replaced by Y. The calculation of the ff energy at location F (E_F) is identical to that given for the small-ρ range described previously.

B.3. Zone 2C

This ff-generation zone, shown in the lower diagram of Fig. 2, is present only for points F in the small-ρ range. As shown in greater detail in Fig. B2, ffs originating at point G in zone 2C initially travel through medium 2, enter medium 1 at point H, exit at point K, and complete their trajectory to point F through medium 2.

This diagram shows one quarter of the circle representing zone 1 and an arc of a dashed circle representing the range of ffs in medium 2 centered on point F. Zone 2C is the shaded area cut off from a direct view of point F by a portion of zone 1. Shown are three rays from point F to the arc AGS, which is the locus of r_{max} for this zone. The formulas for U in Table 3 give the equations needed to determine r_{max} (i.e., GF). Starting from point F, where the ff stops, E_K is obtained from Table 2 for the projected range KF, which is given by Q_- in Table 3. The projected range at point H equals the projected range at point K (both in medium 1) plus the path length $HK = Q_+ - Q_-$. From $PR_1(E_H)$, the energy of the ff at point H is

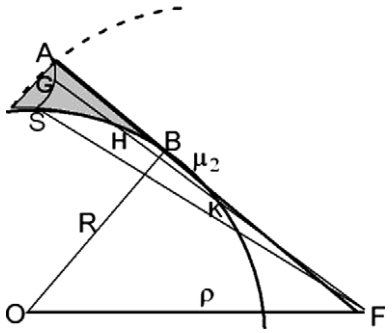

Fig. B2. Trajectories of ffs emitted from zone 2C.

determined from the appropriate SRIM table. The length of the segment GH is the range of the birth-energy ff in medium 2 less the projected range in the same medium at point H, namely $PR_2(E_H)$. Adding the length of $HF = Q_+$ gives, as a function of polar angle φ, the maximum distance in zone 2C from which ffs can reach point F. The locus of these points is the arc AGS.

The angular range of r_{max} in zone 2C begins at $\angle SFO = \cos^{-1} W$. This angle is the same as $\angle HFO$ in Fig. B1, which has been considered above.

B.4. Zones 2A and 2B

The geometry of these two zones is straightforward. X and Y are the cosines of the angles BFO in the diagrams in Fig. 3.

References

[1] J. Turnbull, C. Friskney, F. Findlay, F. Johnson, A. Walter, J. Nucl. Mater. 107 (1982) 168.
[2] Hj. Matzke, Rad. Eff. 64 (1982) 3, see p. 20.
[3] Hj. Matzke, in: R.P. Argawala (Ed.), Diffusion Processes in Nuclear Fuels, Elsevier, 1992, p. 3, see p. 57.
[4] A. Höh, Hj. Matzke, J. Nucl. Mater. 48 (1973) 157.
[5] Hj. Matzke, in: G. Simkovich, V. Stubican (Eds.), Transport in Nonstoichiometric Compounds, Plenum, 1985, p. 331.
[6] D. Olander, Fundamental aspects of nuclear reactor fuel elements, National Technical Information Services, 1976.
[7] J.F. Ziegler, J.P. Biersack, U. Littmark, The Stopping and Range of Ions in Solids, Pergamon, 2003.
[8] N. Chauvin, R. Konings, Hj. Matzke, J. Nucl. Mater. 274 (1999) 105.